Article

Biodegradable copper-iodide clusters modulate mitochondrial function and suppress tumor growth under ultralow-dose X-ray irradiation

Xiaoqian Ma[1,2,3], Nuo Lin[1,2,3], Qing Yang[1,2,3], Peifei Liu[1,2], Haizhen Ding[1,2], Mengjiao Xu[1,2], Fangfang Ren[1,2], Zhiyang Shen[1,2], Ke Hu[1,2], Shanshan Meng[1,2] & Hongmin Chen [1,2] ✉

Both copper ($Cu^{2+/+}$) and iodine (I^-) are essential elements in all living organisms. Increasing the intracellular concentrations of Cu or I ions may efficiently inhibit tumor growth. However, efficient delivery of Cu and I ions into tumor cells is still a challenge, as Cu chelation and iodide salts are highly water-soluble and can release in untargeted tissue. Here we report mitochondria-targeted Cu-I cluster nanoparticles using the reaction of Cu^+ and I^- to form stable bovine serum albumin (BSA) radiation-induced phosphors (Cu-I@BSA). These solve the stability issues of Cu^+ and I^- ions. Cu-I@BSA exhibit bright radioluminescence, and easily conjugate with the emission-matched photo-sensitizer and targeting molecule using functional groups on the surface of BSA. Investigations in vitro and in vivo demonstrate that radioluminescence under low-dose X-ray irradiation excites the conjugated photosensitizer to generate singlet oxygen, and combines with the radiosensitization mechanism of the heavy atom of iodine, resulting in efficient tumor inhibition in female mice. Furthermore, our study reveals that BSA protection causes the biodegradable Cu-I clusters to release free Cu and I ions and induce cell death by modulating mitochondrial function, damaging DNA, disrupting the tricarboxylic acid cycle, decreasing ATP generation, amplifying oxidative stress, and boosting the Bcl-2 pathway.

Hepatocellular carcinoma (HCC) is the most common type of primary liver cancer[1], As a redox-active transition metal, Copper is essential to all living organisms, including liver physiology[2,3]. The interplay of liver physiology and copper metabolism established the relationship between copper homeostasis and the progression of HCC[3–5]. Recent studies clearly revealed that Cu chelation therapy efficiently inhibited tumor growth by increasing the intracellular concentration of Cu ions, which depleted mitochondrial copper and subsequently reduced energy production and inhibited oxidative phosphorylation (OXPHOS) of cancer cells, activating autophagic kinases[6–8] The concept of cuproptosis has been assessed, which depends on mitochondrial respiration and induces cell death by copper overload[9–12]. Intracellular

---

[1]State Key Laboratory of Vaccines for Infectious Diseases, Center for Molecular Imaging and Translational Medicine, Xiang An Biomedicine Laboratory, School of Public Health, Xiamen University, 361102 Xiamen, China. [2]State Key Laboratory of Molecular Vaccinology and Molecular Diagnostics, National Innovation Platform for Industry-Education Integration in Vaccine Research, Xiamen University, 361102 Xiamen, China. [3]These authors contributed equally: Xiaoqian Ma, Nuo Lin, Qing Yang. ✉e-mail: hchen@xmu.edu.cn
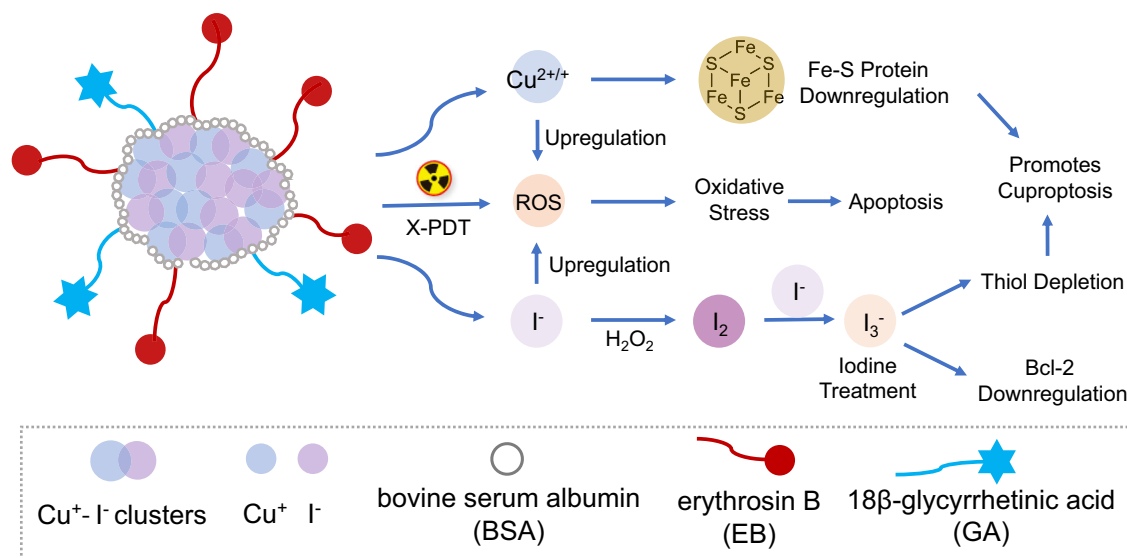
Fig. 1 | Schematic of mechanisms of Cu-I@BSA-EBGA induced cell death. Cu-I@BSA exhibited bright radioluminescence and easily conjugated with the emission-matched photosensitizer erythrosin B (EB) and targeting molecule GA (Cu-I@BSA-EBGA) using functional groups on the surface of BSA. Investigations in vitro and in vivo demonstrated that (1) Cu-I@BSA-EBGA accumulated in tumors via an active-targeting mechanism, and X-ray irradiation in tumor regions generated ROS via the X-PDT process. When combined with the radiosensitization mechanism of the heavy atom iodine, this resulted in efficient tumor inhibition.

(2) Cu-I@BSA-EBGA degraded to free Cu^+ and I^- in the tumor region, both of which reacted with H_2O_2 in tumors to generate $Cu^{2+/+}$ and I_2/I_3^-. This process induced cell death by modulating mitochondrial function, damaging DNA, decreasing ATP generation, and amplifying oxidative stress. (3) Iodine treatment promoted Cuproptosis. A single Cu-I cluster nanoplatform decomposed to Cu^+ and I^- ions, promoting the process of proteotoxic stress, mitochondrial dysfunction, and ultimately, cell death.

Cu^+ ions directly bind to lipoylated TCA cycle proteins to generate a toxic gain-of-function. Efficient delivery of copper ions to tumor cells is still a challenge, as copper ions release in untargeted tissue due to their weak stability under normal biological conditions of Cu chelation.

Iodine is also an essential element in human physiology[13]. Research has revealed evidence that iodine could be employed as an independent influence in the prevention of cancers[14–16]. Iodide (I^-) can act directly as an electron donor to quench free radicals, and indirectly iodinate biomolecules (amino acids, fatty acids). Iodine-biofortified lettuce promoted the mitochondria-dependent pathway of apoptosis in human gastrointestinal cancer cells[17]. Experiments revealed that the antioxidant capacity of molecular iodine (I_2) was 10-fold more potent than that of ascorbic acid and 50-fold more potent than that of potassium iodide[18]. Povidone-iodine (PVP-I_3^-) showed antineoplastic activity in mesothelioma cell lines by inhibiting superoxide dismutase activity through the oxidizing effects of free iodine[19]. Iodine also acted in thiol redox systems, which might help maintain an optimal redox balance in cells[20]. Recent studies suggested that clinical iodinated contrast agents increased radiation-induced cancer cell death[21], and potassium iodide nanoparticles enhanced radiotherapy[22]. Efficiently delivery of iodide ions in tumor cells is still a challenge as iodide salts are highly water solubility and will release in untargeted tissue.

The reaction of copper (Cu^+) and iodide (I^-) forms stable structures that could solve the stability issue of Cu^+ and I^- ions. Studies have shown that the combination of copper (Cu^+)–iodide (Cu-I) clusters with organic ligands resulted in structural diversity with high water stability, low cytotoxicity, and high luminescence efficiency[23,24]. To increase the water stability and luminescence of Cu-I clusters, high-affinity polymers have successfully stabilized and dispersed the anionic Cu-I inorganic units via both coordinative and electrostatic interactions[25]. Cu-I clusters with a high content of iodide emitted high luminescence with a quantum yield up to nearly 100% with light[25]. X-ray-induced photodynamic therapy (X-PDT), utilizing deeply penetrating X-ray irradiation to generate sufficient reactive oxygen species (ROS) to promote anticancer efficacy, has become one of the

prominent modalities for cancer therapy with its minimal invasiveness and high selectivity[26,27]. Nevertheless, the therapeutic effect of X-PDT is compromised by insufficient luminescence productivity and the conversion efficiency of scintillators, which absorb X-rays and transmit energy to photosensitizer[28,29]. Therefore, exploring well-matched energy and high-luminescence scintillators is desirable for enhanced therapeutic efficacy. Two approaches—improving chemical structures and their composition, and increasing luminescence under X-ray irradiation—can benefit the process of X-ray-induced photodynamic therapy[30–33]. A high iodide content could absorb more X-ray photons to increase energy deposition and amplify the generation of free electrons for radio-enhancement. Additionally, high luminescence could amplify the generation of light photons for photodynamic therapy mechanism.

18β-Glycyrrhetinic acid (GA), a pentacyclic triterpenoid extract of licorice, has been widely used as liver targeting ligand, where GA specifically binds to GA receptors, which are abundant on hepatocyte membranes but expressed at a low level on other cells[34–36]. Moreover, GA with mitochondrial targeting capabilities differentiates it from other target molecules[37]. The coupling of GA to Cu-I clusters could enhance accumulation in liver tumors and effectively reduce side effects in normal tissue. However, how to efficiently degrade Cu-I clusters to free Cu^+ and I^- ions in tumors after X-PDT for extended ion therapy is still a challenge because of their insolubility in water.

Here, we show a HCC mitochondria-targeting Cu-I cluster nanoparticle. We introduce bovine serum albumin (BSA) to stabilize the Cu-I cluster (Cu-I@BSA), facilitating excellent dispersibility in water. Cu-I@BSA exhibit bright radioluminescence and easily conjugate with the emission-matched photosensitizer erythrosin B (EB) and the targeting molecule GA (Cu-I@BSA-EBGA) using functional groups on the surface of BSA (Fig. 1). Investigations in vitro and in vivo demonstrate that (1) Cu-I@BSA-EBGA accumulate in tumors via an active-targeting mechanism, and X-ray irradiation in tumor regions generate ROS via the X-PDT process. When combined with the radiosensitization mechanism of the heavy atom iodine, this results in efficient tumor

inhibition. (2) Cu-I@BSA-EBGA degrade to free Cu^+ and I^- in the tumor region, both of which react with H_2O_2 in tumors to generate $Cu^{2+/+}$ and I_2/I_3^-. This process induces cell death by modulating mitochondrial function, damaging DNA, decreasing ATP generation, and amplifying oxidative stress. To our knowledge, there is no report on this application of redox reaction to generate in situ excess intracellular iodine for therapeutic purposes. (3) Iodine treatment promotes Cuproptosis. A single Cu-I cluster nanoplatform decomposes to Cu^+ and I^- ions, promoting the process of proteotoxic stress, mitochondrial dysfunction, and ultimately, cell death. To the best of our knowledge, our design reports a biodegradable Cu-I cluster with nanosize that could generate bright radio-luminescence and release both free Cu and I ions for therapeutic purposes.

Results and discussion

Preparation and characterization of copper-iodide (Cu-I) clusters

Biodegradable copper–iodide (Cu-I) clusters were prepared using the cationic ligand 1-propyl-1,4-diazabicyclo [2.2.2] octan-1-ium (pr-ted) as a stabilizer. The structure of pr-ted was characterized by ^{1}H NMR and ^{13}C NMR (Supplementary Figs. 1–3) to verify the successful synthesis of pr-ted. Bovine serum albumin (BSA) was employed to protect and stabilize the Cu-I nanoparticles (Cu-I@BSA). Cu-I@BSA showed a spherical morphology with a diameter of around 30 nm and hydrodynamic diameter of around 102.4 nm (Fig. 2a). The crystal structure was confirmed as Cu_4I_6(pr-ted)$_2$ cluster (Supplementary Fig. 4)[23,25,32]. The X-ray-excited optical luminescence (XEOL) spectrum showed a sharp and maximal emission peak at 530 nm, which matched well with the absorption of EB (Fig. 2b). Therefore, EB was coupled on Cu-I@BSA (Cu-I@BSA-EB) using the EDC/NHS process (Fig. 2c). To enhance its tumor-targeting ability, the liver-targeting ligand 18β-glycyrrhetinic acid (GA) was further conjugated to Cu-I@BSA-EB (Cu-I@BSA-EBGA) (Fig. 2d). The size of the nanoparticles was almost unchanged (DLS results in Fig. 2c, **d**), but the modifications of EB and GA changed the surface charges from −11.8 mV to −29.7 mV and −24.5 mV, respectively (Fig. 2e). The successful conjugation was further confirmed by UV-vis spectra, infrared spectroscopy analysis, thermogravimetric analysis, ^{1}H NMR spectra (Fig. 2f, Supplementary Figs. 5–7). The XEOL spectra and image results showed that the characteristic emission of Cu-I@BSA almost completely disappeared after the conjugation of EB (Fig. 2g, Supplementary Fig. 8). After successfully confirming the X-ray-excited optical emission, the X-PDT performance was explored by singlet oxygen sensor green (SOSG) as an indicator, which caused the intensity to increase sharply because of the emergence of endoperoxide by $^1O_2$ (Fig. 2h)[38]. Compared with the control groups, Cu-I@BSA-EBGA induced enhanced $^1O_2$ generation under X-ray irradiation (Supplementary Fig. 9).

Because of the protection by the serum albumin protein, Cu-I@BSA-EBGA exhibited excellent colloidal stability in different media under normal conditions (Supplementary Fig. 10). Cu-I@BSA were stable in normal conditions and gradually decomposed to free Cu and I ions in a simulated tumor microenvironment (TME) (acidic environment and high H_2O_2) and generated molecular I_2 (Supplementary Fig. 11). The boosted ion release in the simulated TME generated more hydroxyl (•OH) radicals (Fig. 2i, Supplementary Fig. 12).

Cellular uptake, endocytosis pathway, subcellular internalization and penetration in vitro

Nanoparticles that can target malignant cells may enhance tumor accumulation and mitigate side effects. The cellular uptake performance and endocytosis pathway investigations showed that targeting modifications increased the cellular uptake efficiency of Cu-I@BSA-EBGA compared with Cu-I@BSA-EB (Fig. 3a, Supplementary Figs. 13, 14), and the gating strategy was illustrated in Supplementary Fig. 15. The cellular uptake efficiency of Cu-I@BSA-EBGA increased 2.7-fold

and 2.1-fold after 0.5 h and 2 h incubation, respectively, compared to Cu-I@BSA-EB (Fig. 3b, Supplementary Figs. 13b, 14b). Fluorescent imaging further confirmed the enhancement (Supplementary Fig. 16). The endocytosis pathway investigation of Cu-I@BSA-EBGA indicated both energy-requiring and GA-mediated endocytosis in HepG2 cells (Fig. 3c). 3D multicellular spheroids (MSs) mimic the morphology and microenvironment of tumors[39,40]. In Cu-I@BSA-EBGA treated HepG2 MSs, the fluorescence of EB distributed throughout the entire MS; however, the fluorescence signal of the Cu-I@BSA-EB treated group primarily spread at the periphery of the MSs (Supplementary Fig. 17), contributing to the tumor receptor-mediated uptake behavior of GA. To reveal the cellular localization of Cu-I@BSA-EBGA, HepG2 cells were co-stained with MitoTracker green, LysoTracker red, and Hoechst 33342 after 6 h of exposure to the nanoparticles. The orange fluorescence signal of EB overlapped well with the mitochondria and lysosomes (Fig. 3d, Supplementary Fig. 18). Pearson's colocalization coefficient (R) of Cu-I@BSA-EBGA was 0.71 for mitochondria[34], which was higher than that of Cu-I@BSA-EB (R = 0.55) (Supplementary Fig. 18). UV−vis analysis of intracellular EB concentrations and analysis of Cu concentrations in HepG2 cells after being treated with different concentrations of Cu-I@BSA-EBGA for 6 h indicated a concentration-dependent increase, with a sharp increase observed at a concentration of 5 μg/mL (Supplementary Fig. 19).

Cellular cytotoxicity, colony formation and cell cycle arrest

Compared to unmodified nanoparticles, the targeting modifications induced high tumor cellular cytotoxicity (Fig. 3e, Supplementary Fig. 20). Moreover, GA-modification induced significant cellular uptake efficiency in HepG2 human hepatoma carcinoma cells compare to HCCLM3, MHCC97 human hepatoma carcinoma cells and mouse hepatoma carcinoma cell Hepa1-6 (Supplementary Fig. 21). As GA are high-expressed in human HCC that actively targeted human HCC and achieved high cytotoxicity (Supplementary Fig. 22, Supplementary Table 1). Notably, all the particles showed low cellular cytotoxicity in a normal human fetal hepatocyte line (Supplementary Fig. 23). As expected, Cu-I@BSA-EBGA combined with X-ray irradiation (2 Gy) exhibited the most prominent cell killing efficiency because of the enhanced generation of ROS (Fig. 3e, Supplementary Table 1).

A ROS imbalance is capable of causing cell dysfunction[41]. Cells treated with the four formulations followed by X-ray irradiation inhibited colony formation to different degrees (Fig. 3f). The survival fraction of Cu-I@BSA-EBGA + X-ray-treated HepG2 cells was calculated to be 0.02, which was far lower than that of PBS + X-ray (0.92), Cu-I@BSA + X-ray (0.74), Cu-I@BSA-EB + X-ray (0.28), and Cu-I@BSA-EBGA (0.61) treatments (Fig. 3g). The cell cycle is comprised of G1, G2, S and M phases, among which G2 is the most radiosensitive phase[42,43]. The cell cycle arrest of HepG2 cells after being treated with different formulations showed that Cu-I@BSA-EBGA-treated cells had a 1.8-fold enhancement of the G2 phase proportion compared with the PBS group (Fig. 3h, Supplementary Fig. 24, Supplementary Table 2). Cell cycle arrest in the G2 phase should improve X-PDT efficiency.

The cellular ROS level was investigated using the 2′,7′-dichlorodihydrofluorescein diacetate (DCFH-DA) probe. Cells treated with formulations displayed stronger green fluorescence signals than did the PBS group, which were induced by the released ions (Fig. 4a). Predictably, X-ray irradiation increased the fluorescent signals, and Cu-I@BSA-EBGA with X-ray irradiation exhibited the strongest fluorescent signal because of the production of $^1O_2$ from the X-PDT mechanism (Fig. 4a, Supplementary Fig. 25). The number of singlet oxygen generated based on the irradiation dose was calculated to be $(4.4 \pm 0.5) \times 10^{16}$ $^1O_2$ per Gy (Supplementary Fig. 26)[44–47]. Cellular ROS generation induces cell stress. An analysis of the lipid peroxidation levels revealed that the combination of Cu-I@BSA-EBGA with X-ray irradiation produced the most significant membrane oxidation (Fig. 4b, Supplementary Fig. 27).
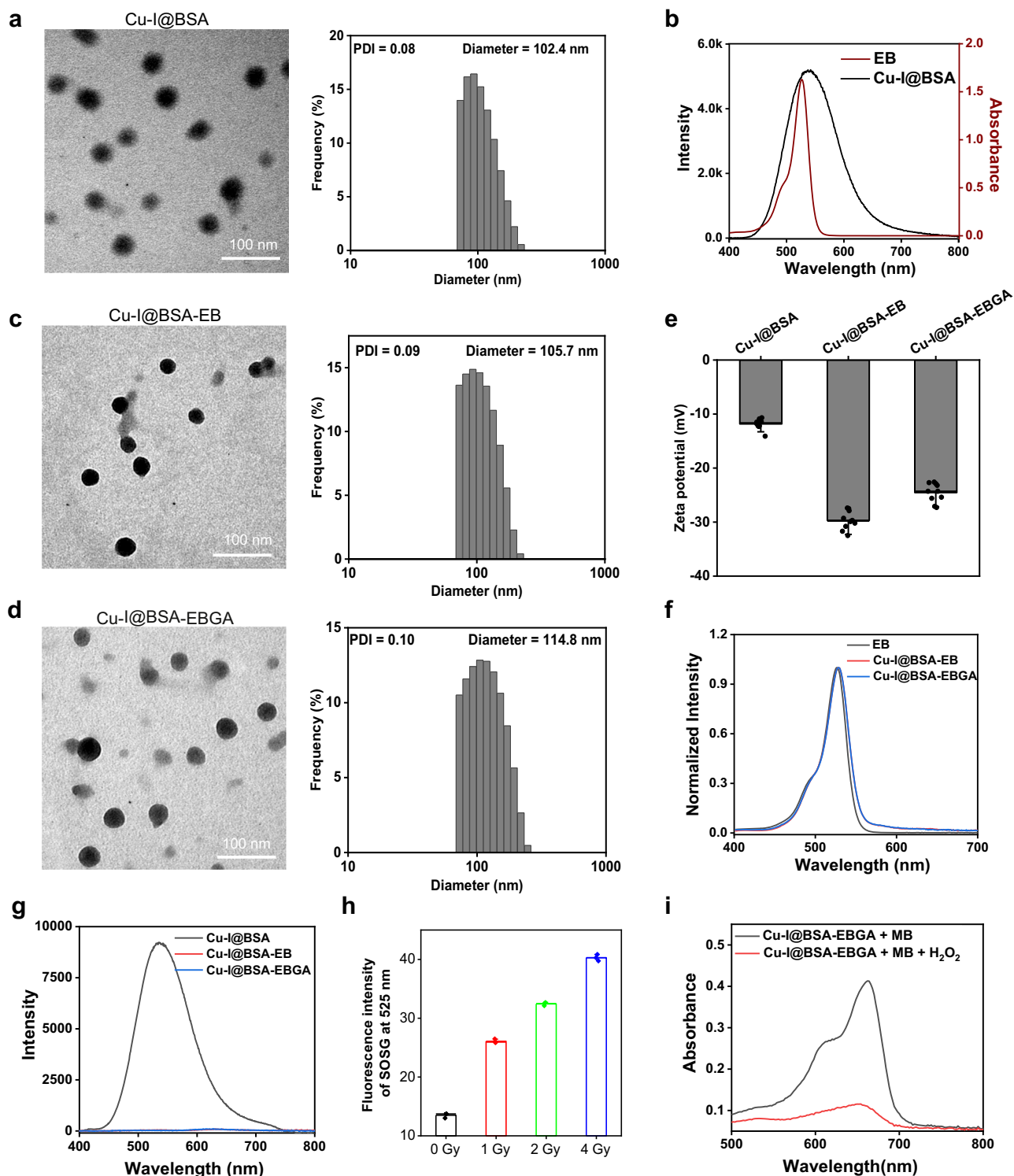
Fig. 2 | Characterizations of biodegradable copper-iodide clusters and their conjugations. a TEM image (left) and DLS analysis (right) of Cu-I@BSA (Scale bar: 100 μm). Experiments were repeated three times independently with similar results. **b** XEOL spectrum of Cu-I@BSA (black curve) and absorbance spectrum of EB (red curve). **c, d** TEM image (left) and DLS analysis (right) of Cu-I@BSA-EB (**c**) and Cu-I@BSA-EBGA (**d**) (Scale bar: 100 μm). Experiments were repeated three times independently with similar results. **e** Zeta potential analysis of copper-iodide clusters and their conjugations ($n = 10$ technical replicates). **f, g** UV–vis spectra (**f**) and XEOL changes (**g**) of Cu-I@BSA, Cu-I@BSA-EB and Cu-I@BSA-EBGA. **h** The generation of singlet oxygen in the presence of Cu-I@BSA-EBGA plus X-ray irradiation ($n = 3$ experimental replicates). **i** The absorbance changes of MB in the presence of Cu-I@BSA-EBGA with/without H_2O_2. Data are presented as mean ± standard deviation (SD) for (**e**) and (**h**).

Excess intracellular iodine is known to deplete the total cellular thiol content and induce apoptosis via the mitochondria-mediated pathway[48,49]. To determine the impact on cellular total thiol content, cells were incubated with Cu-I@BSA-EBGA with or without X-ray irradiation. The total cellular thiol content exhibited a concentration-dependent decrease, and was not influenced by X-ray irradiation (Supplementary Fig. 28), indicating that thiol depletion was mainly caused by the release of iodine ions.
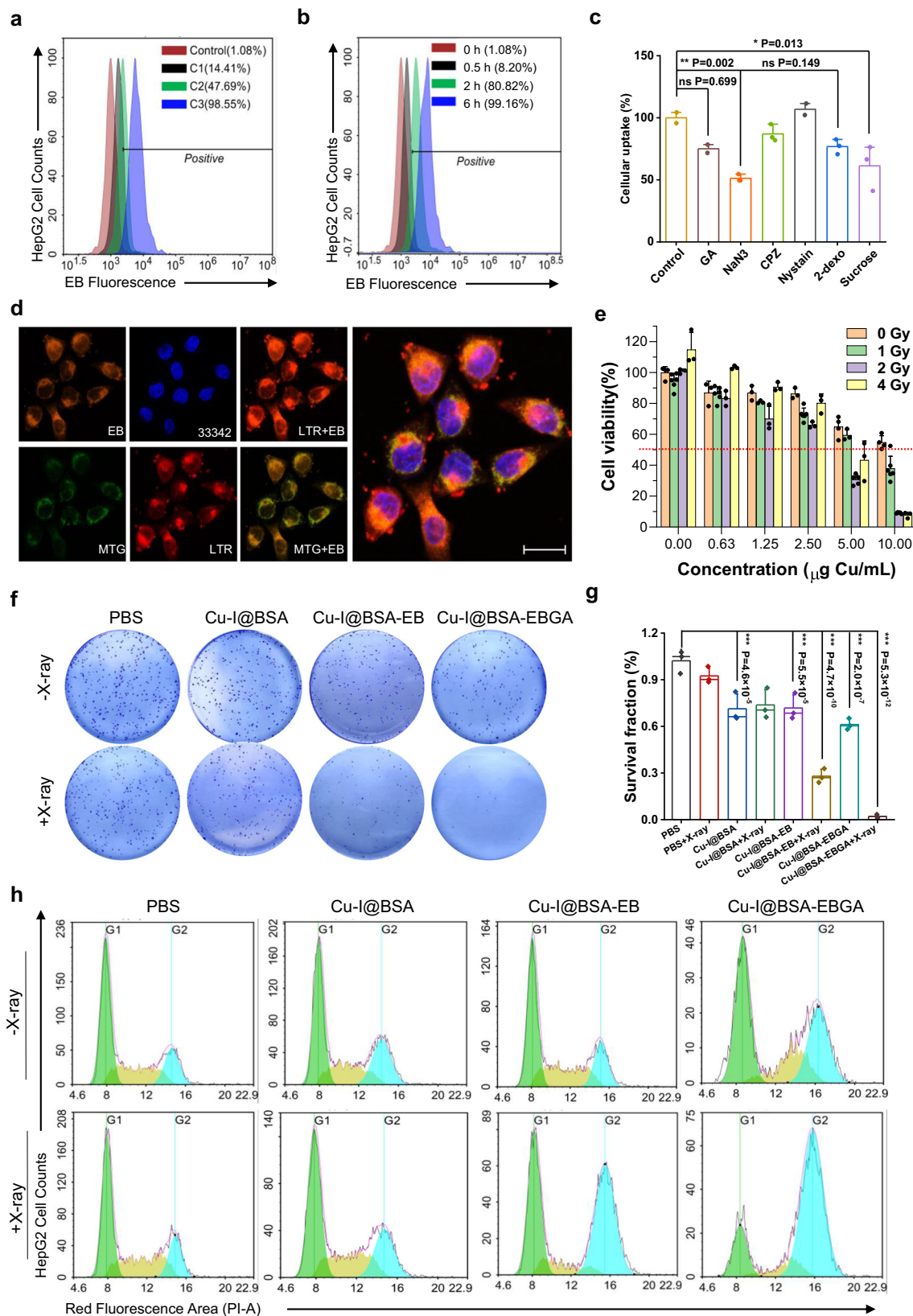
The depolarization of the mitochondrial membrane potential was assessed with the 5,5′,6,6′-tetrachloro-1,1′,3,3′-tetra-ethylimidacarbocyanine (JC-1) fluorescent probe[50,51], and represents the early apoptosis of mitochondria[52]. The analysis showed that the fluorescence of cells after different treatments turned from red (aggregation) to green (monomer) when compared with the control

group (Fig. 4c, Supplementary Fig. 29). The ratio of the monomer to aggregates ranged from 0.13 to 1.05 in Cu-I@BSA-EBGA with X-ray irradiation compared to that of PBS, suggesting activation of the powerful mitochondria-dependent apoptosis pathway. Cellular ATP production decreased to 41.4% after treatment with Cu-I@BSA-EBGA for 6 h, and cells treated with Cu-I@BSA-EBGA and X-ray irradiation

Fig. 3 | Uptake efficiency and cytotoxicity in vitro. a Cellular uptake of Cu-I@BSA-EBGA incubated with HepG2 cell lines (C1: 1.25 μg Cu/mL, C2: 0.63 μg Cu/mL, C3: 0.31 μg Cu/mL). **b** Cellular uptake of Cu-I@BSA-EBGA (1.25 μg Cu/mL) incubated with HepG2 cell lines for 0.5 h, 2 h, and 6 h. **c** Uptake mechanism of Cu-I@BSA-EBGA (*n* = 3 biological replicates). **d** Intracellular localization of Cu-I@BSA-EBGA in HepG2 cells for 6 h (Blue: nuclei, Green: mitochondria, Red: lysosomes. Scale bar: 50 μm). **e** Cell viability of Cu-I@BSA-EBGA with and without X-ray irradiation

(0–4 Gy) (*n* = 3 biological replicates). **f** Representative photographs of colony formation after different treatments. **g** Colony formation fraction of HepG2 cells on 10 Day after treatments (Cu: 10 μg/mL, X-ray: 2 Gy) (*n* = 3 repeated experiments). **h** Cell cycle of HepG2 cells after treatments. Data ware presented as mean ± SD for (**c**), (**e**), and (**g**). Statistical differences were assessed using one-way analysis of variance (ANOVA), and were defined as ns: Not significant, *$P < 0.05$, **$P < 0.01$, and ***$P < 0.001$.
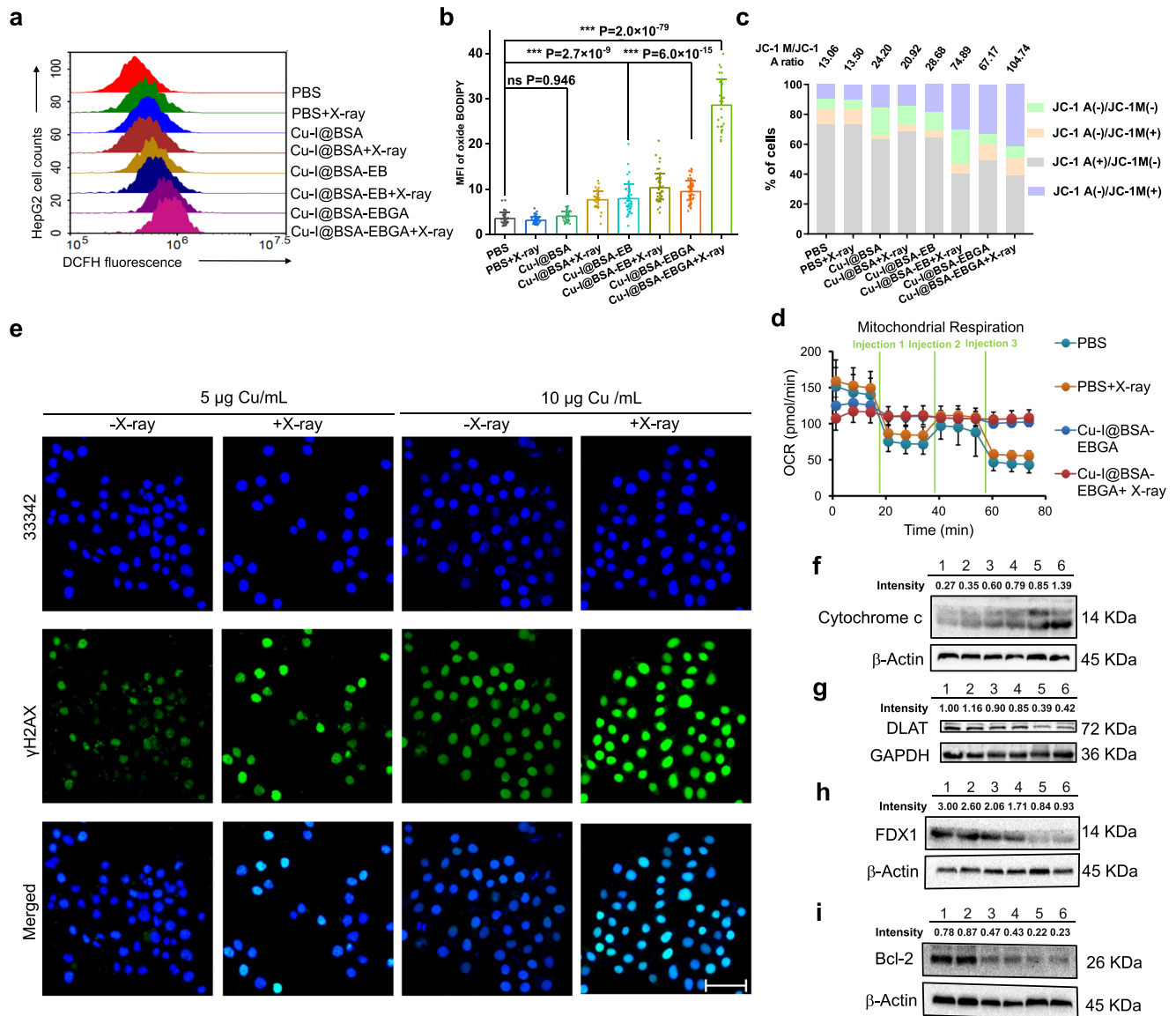

Fig. 4 | Validation of the antitumor mechanism of Cu-I@BSA-EBGA in HepG2 cells. a ROS generation of HepG2 cells after various treatments (5 μg Cu/mL) with or without X-ray irradiation. **b** The lipid peroxidation levels after various treatments (5 μg Cu/mL) with or without X-ray irradiation (*n* = 28 cells). **c** Mitochondrial membrane potential alterations after various treatments (5 μg Cu/mL) with or without X-ray irradiation. JC-1 M: JC-1 Monomer, JC-1 A: JC-1 Aggregation. **d** Oxygen consumption rates of HepG2 cells after different treatments. Injection 1: Oligomycin (5 mM), Injection 2: FCCP (2.5 μM), Injection 3: Rotenone/antimycin A (0.5 μM). (*n* = 3 technical replicates) (**e**) γH2AX staining after various treatments (5 and 10 μg Cu/mL) with or without X-ray irradiation (Scale bar: 50 μm). Experiments

were repeated three times independently with similar results. **f–i** Representative immunoblot analysis of cytochrome c (**f**), DLAT (**g**), FDX1 (**h**), Bcl-2 (**i**) protein levels. Pre-stained protein marker: ColorMixed Protein Marker 180 (10–180 kDa) (Abclonal, RM19001). HepG2 cells after treated with PBS: 1; PBS + X-ray: 2; Cu-I@BSA-EBGA (Cu equivalent dose: 5 μg/mL): 3; Cu-I@BSA-EBGA + X-ray (Cu equivalent dose: 5 μg/mL, X-ray dose: 2 Gy): 4; Cu-I@BSA-EBGA (Cu equivalent dose: 10 μg/mL): 5; Cu-I@BSA-EBGA + X-ray (Cu equivalent dose: 10 μg/mL, X-ray dose: 2 Gy): 6. Experiments were repeated independently with similar results. Data are presented as mean ± SD for (**b**) and (**d**). Statistical differences were assessed using one-way ANOVA, and were defined as ns: Not significant, *$P < 0.05$, **$P < 0.01$, and ***$P < 0.001$.

showed a sharply reduced ATP content of 8.1% compared to that of PBS (Supplementary Fig. 30). Maximum oxygen consumption (OCR), an indicator of OXPHOS, was assessed using a Seahorse XFe96 analyzer. The baseline OCR was first measured before the introduction of inhibitors. Subsequently, oligomycin was added to inhibit ATP

synthase and block ATP generation, and the OXPHOS uncoupling agent carbonyl cyanide 4-(trifluoromethoxy) phenylhydrazone (FCCP) was then added to disrupt ATP synthesis by transporting protons. Last, the inhibitor of the electron transport chain rotenone/antimycin A was injected to determine non-mitochondrial respiration. Only Cu-I@BSA-

EBGA incubation, with or without X-ray irradiation, reprogrammed cellular metabolism (Fig. 4d). The parameters of respiration, including non-mitochondrial oxygen consumption, proton leakage, ATP production, and basal respiration, showed that the OCR for non-mitochondrial oxygen consumption increased sharply in both Cu-I@BSA-EBGA with or without X-ray irradiation. Furthermore, significant decreases were detected in the OCR, ATP production, and basal respiration (Supplementary Fig. 31). On the basis of these results, we concluded that Cu-I@BSA-EB disturbed mitochondrial respiration.

Evaluation of DNA damage and expression of cytochrome c, FDX1 and Bcl-2 protein

The radiation effects of Cu-I@BSA-EBGA were also assessed. The γH2AX levels exhibited concentration- and radiation-related DNA damage (Fig. 3e, Supplementary Fig. 32), with radiation having a greater effect than the nanoparticles did. The optimized staining with high resolution clearly showed that bright and dots signals existed within the nuclei (Supplementary Fig. 33). This was consistent with the colony formation results (Fig. 3f). The treatment effectively enhanced DNA damage levels and further inhibited cell proliferation.

Cytochrome c is a critical protein that regulates cell apoptosis[53,54]. Cells incubated with Cu-I@BSA-EBGA produced a significant release of cytochrome c (Fig. 4f). Notably, X-ray irradiation boosted the release of cytochrome c. Cuproptotic cell death causes aggregation of dihydrolipoyl transacetylase (DLAT) and proteotoxic stress by the binding of copper to lipoylated mitochondrial enzymes (Fig. 4g). The Fe−S cluster protein ferredoxin (FDX1) expression levels in Cu-I@BSA-EBGA and Cu-I@BSA-EBGA + X-ray were downregulated, demonstrating that this treatment effectively destabilized FDX1 and downregulated its expression (Fig. 4h)[55,56].

Bcl-2 is commonly overexpressed in tumors, and is involved in the regulation of apoptosis with a vital role in protecting against cancer[57,58]. Therapeutics targeting Bcl-2 are a valid option for improving or developing cancer treatments. Iodine treatment-induced changes in Bcl-2 family member protein levels, which involved the mitochondria-mediated pathway[48,59]. As a pivotal protein of iodine therapy, Bcl-2 expression was then determined to verify whether iodine treatment was involved in Cu-I@BSA-EBGA + X-ray-induced cell death[48,49,59]. After incubation, only iodine-containing formulations suppressed the expression of Bcl-2 protein (Fig. 4i). The downregulation of Bcl-2 protein was concentration-dependent, and X-ray irradiation further accentuated Bcl-2 downregulation. Taken together, Cu-I clusters were efficiently internalized by HCC cells using their active-targeting mitochondria mechanism. Under low-dose X-ray irradiation, the high loading of iodine in the Cu-I clusters enhanced absorption of X-ray irradiation to generate ROS for radio-enhancement and emit bright luminescence to activate conjugated photosensitizers for the generation of singlet oxygen. Because of the TME (weakly acidic environment and high H_2O_2 levels), Cu-I clusters decomposed to Cu^+ and I^- ions, which promoted the process of proteotoxic stress, mitochondrial dysfunction, and ultimately cell death (Fig. 1).

In vivo biological security, blood circulation, biodistribution and antitumor performance

An analysis of the complete blood count and blood biochemistry indexes showed that Cu-I@BSA-EBGA (5 mg and 20 mg Cu/kg) had notable biocompatibility (Supplementary Figs. 34–36). The good biocompatibility prolonged the blood circulation time, with a blood circulation half-life of 2.2 h (Fig. 5a). The biodistribution of Cu-I@BSA-EBGA in HepG2 tumor-bearing mice showed fluorescence in the tumor tissue that gradually increased and reached a maximum signal after 12 h of administration (Fig. 5b, Supplementary Fig. 37). Ex vivo imaging and quantitative analysis showed a higher accumulation of Cu-I@BSA-EBGA in the tumors compared with other organs (Fig. 5c, Supplementary Fig. 37b), implying excellent tumor-targeting and long

retention ability of Cu-I@BSA-EBGA. The biodistribution of Cu-I@BSA-EBGA in HepG2 tumor-bearing mice showed that fluorescence was higher in the tumor tissue than that of HCCLM3 and HepG1-6 tumor-bearing mice (Fig. 5c, Supplementary Fig. 38).

Encouraged by the prolonged blood circulation and long retention of Cu-I@BSA-EBGA in tumors, we further investigated the feasibility of Cu-I@BSA-EBGA for in vivo liver cancer therapy via intravenous (i.v.) injection. HepG2-bearing BALB/c nude mice were randomly separated into six groups and received i.v. injections of saline or Cu-I@BSA-EB, Cu-I@BSA-EBGA (10 mg/kg Cu) on day 1, and all the X-ray irradiation (1 or 2 Gy) was performed 12 h later (Fig. 5d). Tumor volumes were measured and analyzed every two days (Fig. 5e). The relative tumor volumes of mice in the PBS, PBS + 1 Gy, PBS + 2 Gy, Cu-I@BSA-EBGA, Cu-I@BSA-EBGA + 1 Gy, and Cu-I@BSA-EBGA + 2 Gy treatment groups were calculated as 10.8, 10.6, 10.5, 5.2, 3.0, and 1.1 on day 14, respectively (Fig. 5f). Only X-ray irradiation alone (1 or 2 Gy) appeared to produce negligible tumor inhibition, Cu-I@BSA-EB induced an anticancer effect with tumor inhibition of 39.4% and 75.3% in the presence of X-ray irradiation (2 Gy) (Supplementary Fig. 39), while Cu-I@BSA-EBGA induced an anticancer effect with a tumor inhibition of 59.4% due to the generation of copper and iodine ions (Fig. 5g). X-ray irradiation improved the antitumor efficiency, and the tumor inhibition rates of Cu-I@BSA-EBGA with 1 Gy or 2 Gy X-ray irradiation increased to 75.2% and 91.6%, respectively (Fig. 5g).

Typical photographs of the extracted tumors and weights further confirmed the antitumor efficiency (Fig. 5h, Supplementary Fig. 40). The efficiency was further confirmed by analyzing the morphology and progression of tumor tissues via hematoxylin and eosin (H&E) staining (Fig. 5i). Compared with the other five groups, Cu-I@BSA-EBGA + 2 Gy treated tumors showed loosely packed cells and few nucleus counts (Supplementary Fig. 41). Moreover, Cu-I@BSA-EBGA with X-ray irradiation neither triggered significant decreases in the body weight of mice (Supplementary Fig. 42) nor caused noticeable damage to major organs (Supplementary Fig. 43), further indicating that Cu-I@BSA-EBGA did not cause acute toxicity.

In summary, we engineered biodegradable copper−iodide clusters using the reaction of Cu^+ and I^- to form stable BSA radiation-induced phosphors (Cu-I@BSA) that solved the stability issues of Cu^+ and I^- ions. Cu-I@BSA exhibited bright radioluminescence, and easily conjugated with the emission-matched photosensitizer EB and targeting molecule GA using functional groups on the surface of BSA. Investigations in vitro and in vivo demonstrated that radioluminescence under low-dose X-ray irradiation excite the conjugated EB to generate singlet oxygen ($^1O_2$), and combined with the radiosensitization mechanism of the heavy atom iodine, resulting in efficient tumor inhibition. Furthermore, our study revealed that BSA protection also caused the Cu-I clusters to biodegrade, increasing the intracellular concentrations of Cu and I ions and inducing cell death by modulating mitochondrial function, amplifying oxidative stress, and boosting the Bcl-2 pathway. Our design may broad the clinical application for cancer treatment in which copper and iodide induce cell death by modulating mitochondrial function under low-dose X-ray irradiation.

Methods

All animal experiments were carried out according to the criteria approved by Institutional Animal Care and Use Committee (IACUC) at Xiamen University.

Synthesis of 1-propyl-1,4-diazabicyclo [2.2.2] octan-1-ium (pr-ted)

The synthesis of pr-ted was conducted following procedure. 1.23 g 1-bromopropane (10 mmol) was added dropwise into 50 mL of acetone containing 1.12 g Ted (10 mmol) under magnetic stirring, the mixture was allowed to react for 1 h at room temperature. With that, the
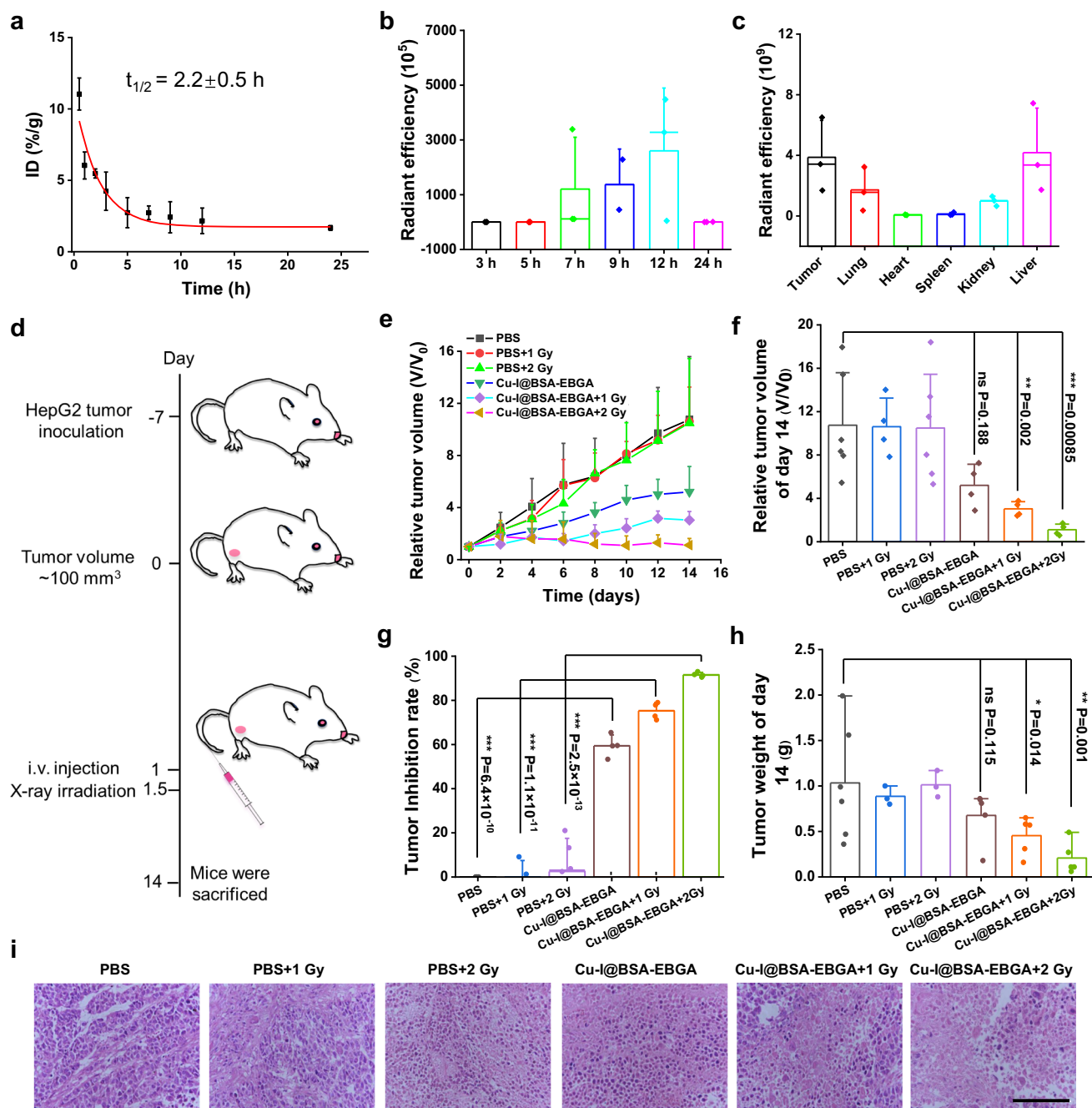
Fig. 5 | In vivo investigation of the antitumor efficiency. a The time-dependent distribution of Cu-I@BSA-EBGA in plasma within 24 h. **b** The tumor fluorescence intensity changes at different time points after tail vein injection of Cu-I@BSA-EBGA. **c** The fluorescence intensities of major organs of mice sacrificed at 24 h post-injection of Cu-I@BSA-EBGA. **d** Illustration of in vivo therapy process. **e** Tumor volume changes of HepG2-tumor bearing mice after different treatments. V represents the tumor volume at different time points, and V_0 represents the tumor volume at Day 0. **f** Tumor volumes on Day 14 after treatments. V represents the tumor volume at different time points, and V_0 represents the tumor volume at Day 0. **g, h** Tumor inhibition rates were calculated using tumor volumes (**g**) and tumor weights (**h**) on Day 14 after the treatments (*n* = 6 mice/group). **i** Representative H&E staining images of tumor tissues after different treatments (Scale bar: 50 μm). Data are presented as mean ± SD for (**a**–**c**) and (**e**–**h**). Statistical differences were assessed using one-way ANOVA, and were defined as ns: Not significant, *P < 0.05, **P < 0.01, and ***P < 0.001.

formative solution was centrifugated (9510 g, 10 min) and washed with ethyl acetate for three times, the pr-ted ligand was acquired after drying under vacuum.

Preparation of copper-iodide clusters

Firstly, 28.5 mg of CuI (0.15 mmol) was dissolved in 0.2 mL of KI-saturated aqueous solution under conditions with ultrasonic, the obtained CuI/KI mixture was added dropwise to 30 mL of ultrapure water containing 0.3 g BSA, following by addition of the mixture of 44 mg pr-ted (0.34 mmol) and 0.1 mL ethyl alcohol, the reaction was placed in dark and continuously stirred for 12 h at room temperature. At the end of the reaction, the resulting mixture was allowed to stand for 1 h to remove the large-size nanoparticles, the supernatant was subjected to centrifugate at 95 *g* for 10 min, and the obtained deposition was further washed with deionized water and ethanol to give Cu-I@BSA.

Modification of EB and GA

Firstly, the photosensitizer EB was grafted by substitution reaction, the obtained Cu-I@BSA deposition was dispersed in 5 mL water was introduced after EDC/NHS activated EB, the mixture was allowed to react at room temperature for 12 h, the impurities in which were removed by three times of washing with deionized water, then Cu-I@BSA-EB was obtained. The target molecular GA was subjected to Cu-I@BSA-EB to prepare Cu-I@BSA-EBGA.

Reactive oxygen species (ROS) generation

The as-prepared Cu-I@BSA-EBGA were dispersed in a PBS 7.4 solution, after introducing 1 mg/mL MB aqueous solution, the resulting mixture was placed into a constant temperature oscillator (37 °C) in the dark, and then the absorbance of MB was detected to analyze the generation of hydroxyl radicals under different conditions. The singlet oxygen generation ability of Cu-I@BSA-EBGA under X-ray irradiation (50 kV and 160 kV) was monitored by a singlet oxygen sensor green (SOSG) fluorescent probe. Cu-I@BSA-EBGA aqueous solution containing 5 µM SOSG probe was prepared. Afterward, the fluorescence emission of SOSG was recorded by a multifunctional enzyme marker.

Cell culture and incubation

Normal human liver cell lines LO2, human hepatoma carcinoma cell lines HepG2, MHCC97, and HCCLM3, mouse-derived hepatoma carcinoma cell lines Hepa1-6 were used in the following experiment. The two kinds of cells were incubated at 37 °C in an incubator (Thermo Scientific) with 5% CO_2. The cell culture medium consists of Dulbecco's modified eagle medium (DMEM), FBS (10%), penicillin, and streptomycin (1%).

Cellular uptake

In response to Cu-I@BSA-EB and Cu-I@BSA-EBGA uptake, 2×10^5 HepG2 cells were seeded into a flat-bottomed 24-well plate and attached at 37 °C overnight. Cell medium containing Cu-I@BSA-EB or Cu-I@BSA-EBGA were added and further incubated for different time intervals, subsequently, the cells of each well were collected and suspended in 300 µL PBS for fluorescence intensity analysis of EB.

The cellular uptake behavior of Cu-I@BSA-EB and Cu-I@BSA-EBGA against HepG2 cells over time was also studied by CLSM. To specific, HepG2 cells (2×10^5) were seeded into a confocal dish and cultured for 12 h, then cells were treated with Cu-I@BSA-EB and Cu-I@BSA-EBGA for 0.5, 2, and 6 h, followed by staining the nucleus with 10 ug/mL Hoechst 33342, the cellular fluorescence intensity was recorded by CLSM 880.

We further investigated the cellular uptake behavior of Cu-I@BSA-EBGA against different hepatoma carcinoma cell lines. HepG2, MHCC97, HCCLM3, and Hepa1-6 cells were planted in a 6-well culture dish with a density of 1×10^6 per well. Cells were treated with different concentrations of Cu-I@BSA-EBGA (5 µg/mL) for 0.5 h. After being rinsed, collected and dispersed, the cellular fluorescence intensity of EB was detected by flow cytometry.

Endocytosis pathway

To study the cellular uptake pathway of Cu-I@BSA-EBGA, HepG2 cells (2×10^5) were planted and preincubated with basal culture medium diluted GA (20×10^{-6} M), sodium azide (NaN_3, 5 mg/mL), chlorpromazine (CPZ, 10 µg/mL), 2-deoxy-D-glucose (2-DG, 8 mmol/L), and sucrose (450 mM) for 1 h at 37 °C, after exposed to Cu-I@BSA-EBGA suspension (Cu equivalent dose: 1.25 µg/mL) and interacted for 2 h, the intracellular fluorescence intensity of EB was quantified by flow cytometry with 1×10^4 ungated cells.

Penetration of nanoparticles in 3D multicellular spheroids (MSs)

A 1% mass fraction of agarose (50 µL) was added in a 96-well plate and sterilized for 1 h, then 1×10^3 HepG2 cells were seeded and incubated at 37 °C for 7 days to obtain MSs. MSs were treated with Cu-I@BSA-EB or Cu-I@BSA-EBGA (Cu equivalent dose: 5 µg/mL) for 8 h, after being transferred into confocal dishes and rinsed with PBS for three times, the penetration behavior was monitored by a CLSM 880 using Z-stack. Images were collected every 10 µm from the bottom to the top of the MSs.

Subcellular localization evaluation

The subcellular distribution of Cu-I@BSA-EB and Cu-I@BSA-EBGA was evaluated by co-localization analysis of EB and commercially available probe-stained subcellular organelles. Briefly, HepG2 cells were seeded into confocal dishes with a density of 2×10^5 per well, after being incubated with Cu-I@BSA-EB and Cu-I@BSA-EBGA for 6 h, cells were stained with mito-tracker green, lyso-tracker red and Hoechst 33342. And then the confocal images were recorded.

Cellular content of EB and copper

1×10^6 cells were seeded and incubated with different concentrations of Cu-I@BSA-EBGA (10, 5, 2.5, 1.25, 0.63 µg/mL) for 6 h. Then, cells were collected and washed three times with cold PBS. The intracellular EB and copper were measured by UV-vis and ICP-MS, respectively.

Cytotoxicity assessment

Cell viability of different formulations against HepG2 cells and LO2 cells was determined by 2-(2-methoxy-4-nitrophenyl)-3-(4-nitrophenyl)-5-(2,4-disulfophenyl)-2h-tetrazolium sodium salt (CCK8) assay. Cells were seeded into a 96-well plate (10^4 cells/well) and incubated in DMEM overnight, after exposure to different concentrations of nanoparticles suspension for 6 h, the medium was substituted with fresh DMEM and cells were irradiated under 2 Gy using an RS-2000 X-ray irradiator (USA). Followed by incubation for 12 h, 10 µL of CCK8 was added and incubated at 37 °C for 1 h, the absorbance at 450 nm was recorded by a multimode reader.

Colony formation assay

The cell proliferation capacity was studied with colony formation assay. Specifically, cells pretreated with PBS, PBS + X-ray, Cu-I@BSA, Cu-I@BSA + X-ray, Cu-I@BSA-EB, Cu-I@BSA-EB + X-ray, Cu-I@BSA-EBGA and Cu-I@BSA-EBGA + X-ray (Cu equivalent dose: 10 µg/mL, X-ray dose: 2 Gy) were rinsed, digested and suspended in fresh DMEM at a low density (approximately 500 cells per milliliter), and then 2 mL of the suspensions were added in a 6-wells plate and cultured for 10 days in an incubator with 5% CO_2. After removing the medium, 50 µL of crystal violet (4%) was added to stain the formative cell clusters for 15 min. The plate was imaged, and the discrete colonies of each well were counted with the naked eye.

Cell cycle arrest

1×10^6 HepG2 cells were seeded into a 6-wells plate and treated with PBS, PBS + X-ray, Cu-I@BSA, Cu-I@BSA + X-ray, Cu-I@BSA-EB, Cu-I@BSA-EB + X-ray, Cu-I@BSA-EBGA and Cu-I@BSA-EBGA + X-ray (Cu equivalent dose: 10 µg/mL, X-ray dose: 2 Gy), then cells were harvested and fixed overnight with absolute ethyl alcohol at 4 °C. After staining the permeabilized cells with PI/Rase staining buffer in accordance with the instruction, the DNA contents of 2×10^5 cells were analyzed by a flow cytometry with PI channel. The cell cycle fitting was according to PI fluorescence with ACEA NovoExpress software.

Intracellular ROS generation

In order to study the intracellular ROS production by PBS, PBS + X-ray, Cu-I@BSA, Cu-I@BSA + X-ray, Cu-I@BSA-EB, Cu-I@BSA-EB + X-ray,

Cu-I@BSA-EBGA and Cu-I@BSA-EBGA + X-ray (Cu equivalent dose: 10 μg/mL, X-ray dose: 2 Gy), 2×10^5 HepG2 cells were seeded and attached for 12 h. After being treated with different formulations for a certain time, cells were stained with DCFH-DA (0.1 μM) fluorescent probe for 30 min in a CO_2 incubator. Finally, the cellular fluorescence intensity of DCFH was detected by flow cytometry. Additionally, the ROS generation ability was also studied on CLSM.

Lipid peroxidation (LPO) elucidation

To investigate the LPO level, HepG2 cells (approximately 2×10^5 cells per dish) were pretreated with PBS, PBS + X-ray, Cu-I@BSA, Cu-I@BSA + X-ray, Cu-I@BSA-EB, Cu-I@BSA-EB + X-ray, Cu-I@BSA-EBGA and Cu-I@BSA-EBGA + X-ray (Cu equivalent dose: 10 μg/mL, X-ray dose: 2 Gy), followed by staining with 10 μM C11-BODIPY581/591 probe (30 min) and 10 μg/mL Hoechst 33342 (15 min), the cells were rinsed and observed on a CLSM 880 with plan-apochromat ×40 objective.

Intracellular thiol depletion

To determine the cellular total thiol content, 1×10^6 HepG2 cells were seeded into a 6-well plate and attached for 12 h, after being treated with PBS, PBS + X-ray, Cu-I@BSA-EBGA (5 μg/mL Cu), Cu-I@BSA-EBGA + X-ray (5 μg/mL Cu, 2 Gy), Cu-I@BSA-EBGA (10 μg/mL Cu) and Cu-I@BSA-EBGA + X-ray (10 μg/mL Cu, 2 Gy), cells were digested, counted and determined the thiol contents in the group of blank, standard samples and materials in accordance with the manufacturer's protocol.

Mitochondrial membrane potential (MMP) assessment

The MMP alteration was detected by using a JC-1 staining kit. 2×10^5 HepG2 cells were seeded and treated with PBS, PBS + X-ray, Cu-I@BSA, Cu-I@BSA + X-ray, Cu-I@BSA-EB, Cu-I@BSA-EB + X-ray, Cu-I@BSA-EBGA and Cu-I@BSA-EBGA + X-ray (Cu equivalent dose: 5 μg/mL, X-ray dose: 2 Gy), then cells were digested and suspended in 200 μL PBS containing JC-1 dye (2 μM of working concentration), after stained at 37 °C for 30 min, the samples were analyzed by flow cytometry. JC-1 aggression features with a high membrane potential and emits red fluorescence, is excited by PI channel, while JC-1 monomer features with a low membrane potential and emit green fluorescence, is emitted by FITC channel.

Intracellular ATP content

The intracellular ATP was detected using an ATP determination kit. In brief, HepG2 cells were seeded into a six-wells plate with a density of 1×10^6 per well, after being attached for 12 h, the cells were treated with PBS, PBS + X-ray, Cu-I@BSA-EBGA, Cu-I@BSA-EBGA + X-ray, respectively. The cellular concentration of ATP was determined in accordance with the manufacturer's protocol of the ATP assay kit.

Determination of mitochondrial respiration

Mitochondrial respiration was evaluated by a seahorse XF analyzer (Agilent XF96, USA). Typically, on the day following HepG2 cell seeding into Seahorse XF96 microplate (1×10^4 cells per well), cells were incubated with Cu-I@BSA-EBGA (10 μg/mL Cu) or PBS for 6 h and further treated with X-ray (2 Gy). Cells were rinsed with $1 \times$ D-PBS for three times and equilibrated in an incubator for 37 °C, the oxygen concentration in media was determined at basal conditions and after treated sequentially with oligomycin (5 mM), FCCP (2.5 μM) and rotenone/antimycin A (0.5 μM).

Western blot

The cellular expression of the relevant protein was studied by Western blot. HepG2 cells were seeded into a flat round 6-well plate (10^6 cells/well) and attached overnight. After being treated with different formulations, cells were collected and rinsed with PBS. Then cells were lysed with preprepared RIPA buffer on ice, the concentrations of

protein were quantified by BCA Protein Quantification Kit (Thermo Scientific). After 10 min of denaturation at 100 °C, equivalent protein was separated by BeyoGel™ Plus Precast PAGE gel (Tris-Gly, 12%, 10 wells, P0458S) and transferred onto immobilon-p PVDF transfer membrane (0.45 μm filter). 3% (w) of BSA was used to block the membrane for 2 h, the membrane was further interacted with the primary antibody for 12 h at 4 °C under successive shaking. Subsequently, secondary antibody was introduced and incubated for 45 min, the Western blot images were visualized with chemiluminescent detection equipment. The primary antibodies used in this study including ADX, Bcl-2, cytochrome c, β-Actin and anti DLAT. Pre-stained protein marker: ColorMixed Protein Marker 180 (10-180 kDa) (Abclonal, RM19001).

Animals

Female BALB/c or BALB/c nude mice (5–6 weeks old) were purchased Beijing Vital River Laboratory Animal Technology Co., Ltd. (China) and Shanghai SLAC Laboratory Animal Co., Ltd. The mice were housed in the Laboratory Animal Center of Xiamen University. To establish HepG2, HCCLM3, Hepa1-6 tumor-bearing mice, 100 μL of cell suspension were injected into the right flank of BALB/C nude mice subcutaneously, the experiment was performed after 7 days of inoculation. The maximum allowable tumor diameter, as specified by the ethics committee, is 1.5 cm. Tumor-bearing mice euthanized when the tumor reached 1.5 cm in diameter or when they became moribund with severe weight loss.

Toxicology evaluation

The blood compatibility of Cu-I@BSA-EBGA was assessed through complete blood count evaluation and blood biochemistry measurement. The healthy BALB/c mice were separated into three groups (n = 3) and intravenously injected with 200 μL of PBS, Cu-I@BSA-EBGA (5 mg/kg Cu) and Cu-I@BSA-EBGA (20 mg/kg Cu). Blood samples were collected from mice eyeballs after 7 days of injection for subsequent analysis. White blood cells (WBC), red blood cells (RBC), hemoglobin (HGB), hematocrit (HCT), mean corpuscular hemoglobin concentration (MCHC) and platelets (PLT) were determined with an automated hematology analyzer (Mindary, China). Alkaline phosphatase (ALP), serum albumin (ALB), aspartate aminotransferase (AST), aminotransferase (ALT), lactate dehydrogenase (LDH) and UREA were quantified using a Mindary automatic biochemical analyzer (BS-220).

Blood circulation

To study the blood circulation profile, BALB/c nude mice were intravenously injected with 200 μL of Cu-I@BSA-EBGA (Cu equivalent dose: 5 μg/mL). Thereafter, blood was withdrawn from mice eye ball at 0.5, 1, 2, 3, 5, 7, 9, 12 and 24 h post-injection and preserved in weighing centrifuge tubes, the amount of Cu in blood samples was measured by an ICP-MS after digestion (HNO_3 and H_2O_2), dilution (ultrapure water) and filtration (0.22 μm mixed cellulose filter).

Fluorescence imaging in vivo

To investigate the in vivo distribution of Cu-I@BSA-EBGA, tumor-bearing mice were intravenously injected with 200 μL of Cu-I@BSA-EBGA (Cu equivalent dose: 5 μg/mL). At predetermined time points, the fluorescence images of mice and Cu-I@BSA-EBGA suspensions were recorded by an imaging system (IVIS Lumia III, Caliper, USA) with the excitation wavelength of 520 nm (λ_{em} = 570 nm), the mice were sacrificed at 24 h post injection, tumors and main organs of mice were collected for ex vivo fluorescent imaging.

Antitumor efficacy study in vivo

10^6 HepG2 cells were inoculated on the right leg of 5~6 weeks-old nude mice. When the tumor volume reached 100 mm³, the mice were

randomly separated into six groups (PBS, PBS + 1 Gy, PBS + 2 Gy, Cu-I@BSA-EBGA, Cu-I@BSA-EBGA + 1 Gy, Cu-I@BSA-EBGA + 2 Gy, 6 mice per group) and intravenously administered at an equivalent Cu dose of 10 mg/kg on day 1, after 12 h of administration, the irradiation was completed under the condition of a voltage of 160 kV and a current of 25 mA. During the treatment, mice weight and tumor size were recorded every two days on day 14, mice of each group were sacrificed and tumors were collected, snapped, and weighed. The tumor tissues stored in a 10% formalin solution were used for HE staining.

Statistics and reproducibility

All statistical analyses were performed by OriginPro 2018, GraphPad Prism 9 or SPSS statistics 24.0, and values were expressed as mean ± standard deviation (SD). Statistical differences were assessed using one-way analysis of variance (ANOVA), and were defined as *$P < 0.05$, **$P < 0.01$ and ***$P < 0.001$. The flow cytometry data were processed using NovoExpress (version 1.5).

The experiments in this study were repeated 3 times independently with similar results unless otherwise noted. No statistical method was used to predetermine the sample size. The investigators were double-blinded to allocation during experiments and outcome assessment.

Reporting summary

Further information on research design is available in the Nature Portfolio Reporting Summary linked to this article.

Data availability

The authors declare that the data supporting the findings of this study are available within the Article and its Supplementary Information Files or from the corresponding author upon request. Source data are provided with this paper.

References

1. Llovet, J. M. et al. Hepatocellular carcinoma. *Nat. Rev. Dis. Primers* **7**, 6 (2021).
2. Ge, E. J. et al. Connecting copper and cancer: from transition metal signalling to metalloplasia. *Nat. Rev. Cancer* **22**, 102–113 (2022).
3. Wu, Z. et al. Copper in hepatocellular carcinoma: a double-edged sword with therapeutic potentials. *Cancer Lett.* **571**, 216348 (2023).
4. Ozkan, E. & Bakar-Ates, F. Cuproptosis as the new kryptonite of cancer: a copper-dependent novel cell death mechanism with promising implications for the treatment of hepatocellular carcinoma. *J. Cancer Res. Clin. Oncol.* **149**, 17663 (2023).
5. Wachsmann, J., & Peng, F. Molecular imaging and therapy targeting copper metabolism in hepatocellular carcinoma. *World J. Gastroenterol.* **22**, 221–231 (2016).
6. Cui, L. et al. Mitochondrial copper depletion suppresses triple-negative breast cancer in mice. *Nat. Biotechnol.* **39**, 357–367 (2021).
7. Ramchandani, D. et al. Copper depletion modulates mitochondrial oxidative phosphorylation to impair triple negative breast cancer metastasis. *Nat. Commun.* **12**, 7311 (2021).
8. Tsang, T. et al. Copper is an essential regulator of the autophagic kinases ULK1/2 to drive lung adenocarcinoma. *Nat. Cell Biol.* **22**, 412–424 (2020).
9. Tsvetkov, P. et al. Copper induces cell death by targeting lipoylated TCA cycle proteins. *Science* **375**, 1254–1261 (2022).
10. Gong, N. et al. Carbon-dot-supported atomically dispersed gold as a mitochondrial oxidative stress amplifier for cancer treatment. *Nat. Nanotechnol.* **14**, 379–387 (2019).
11. Zhou, J. et al. Photothermally triggered copper payload release for cuproptosis-promoted cancer synergistic therapy. *Angew. Chem. Int. Ed.* **62**, e202213922 (2023).
12. Wu, W. et al. Enhanced tumor-specific disulfiram chemotherapy by in situ Cu(2+) chelation-initiated nontoxicity-to-toxicity transition. *J. Am. Chem. Soc.* **141**, 11531–11539 (2019).
13. Nedić, O. Iodine: physiological importance and food sources. *eFood* **4**, e63 (2023).
14. Zhen, X. et al. Potassium iodide enhances the anti-hepatocellular carcinoma effect of copper-cysteamine nanoparticle mediated photodynamic therapy on cancer treatment. *Mater Today Phys.* **27**, 100838 (2022).
15. Venturi, S. et al. A new hypothesis: iodine and gastric cancer. *Eur. J. Cancer Prev.* **2**, 17–23 (1993).
16. Kaczor, T. Iodine and Cancer-A summary of the evidence to date. https://www.naturalmedicinejournal.com/journal/iodine-and-cancer.
17. Sularz, O., Koronowicz, A., Smolen, S., Boycott, C. & Stefanska, B. Iodine-biofortified lettuce can promote mitochondrial dependent pathway of apoptosis in human gastrointestinal cancer cells. *Int. J. Mol. Sci.* **24**, 9869 (2023).
18. Aceves, C., Anguiano, B. & Delgado, G. The extrathyronine actions of iodine as antioxidant, apoptotic, and differentiation factor in various tissues. *Thyroid* **23**, 938–946. (2013).
19. Fiorelli, A. et al. Antineoplastic activity of povidone-iodine on different mesothelioma cell lines: results of in vitro study. *Eur. J. Cardiothorac. Surg.* **45**, 993–1000 (2014).
20. Nowak, B. P., Schlichter, L. & Ravoo, B. J. Mediating oxidation of thioethers with iodine—a mild and versatile pathway to trigger the formation of peptide hydrogels. *Angew. Chem. Int. Ed.* **61**, e202201791 (2022).
21. Wang, L. et al. Enhanced radiation damage caused by iodinated contrast agents during CT examination. *Eur. J. Radiol.* **92**, 72–77 (2017).
22. Cline, B. L. et al. Potassium iodide nanoparticles enhance radiotherapy against breast cancer by exploiting the sodium-iodide symporter. *ACS Nano* **15**, 17401–17411 (2021).
23. Liu, W. et al. All-in-one: achieving robust, strongly luminescent and highly dispersible hybrid materials by combining ionic and coordinate bonds in molecular crystals. *J. Am. Chem. Soc.* **139**, 9281–9290 (2017).
24. Troyano, J., Zamora, F. & Delgado, S. Copper(i)–iodide cluster structures as functional and processable platform materials. *Chem. Soc. Rev.* **50**, 4606–4628 (2021).
25. Wang, J.-J. et al. Highly luminescent copper iodide cluster based inks with photoluminescence quantum efficiency exceeding 98. *J. Am. Chem. Soc.* **142**, 3686–3690 (2020).
26. Lucky, S. S., Soo, K. C. & Zhang, Y. Nanoparticles in photodynamic therapy. *Chem. Rev.* **115**, 1990–2042 (2015).
27. Wang, X. et al. Organic phosphorescent nanoscintillator for low-dose X-ray-induced photodynamic therapy. *Nat. Commun.* **13**, 5091 (2022).
28. Fan, W. et al. Overcoming the Achilles' heel of photodynamic therapy. *Chem. Soc. Rev.* **45**, 6488–6519 (2016).
29. Yu, X. et al. CT/MRI-guided synergistic radiotherapy and x-ray inducible photodynamic therapy using Tb-doped Gd-W-nanoscintillators. *Angew. Chem. Int. Ed.* **58**, 2017–2022 (2019).
30. Liu, X. et al. Lanthanide(III)-Cu4I4 organic framework scintillators sensitized by cluster-based antenna for high-resolution x-ray imaging. *Adv. Mater.* **35**, 2206741 (2023).
31. Zhao, W., Wang, Y., Guo, Y., Suh, Y. D. & Liu, X. Color-tunable and stable copper iodide cluster scintillators for efficient x-ray imaging. *Adv. Sci.* **10**, 2205526 (2023).
32. Wang, Y. et al. Efficient X-ray luminescence imaging with ultra-stable and eco-friendly copper(I)-iodide cluster microcubes. *Light Sci. Appl.* **12**, 155 (2023).

33. Hu, Q. et al. Highly effective hybrid copper(I) iodide cluster emitter with negative thermal quenched phosphorescence for x-ray imaging. *Angew. Chem. Int. Ed.* **62**, e202217784 (2023).

34. Lin, X. et al. Targeting the opening of mitochondrial permeability transition pores potentiates. *Adv. Sci.* **8**, 2002834 (2021).

35. Stankovich, S. et al. Graphene-based composite materials. *Nature* **442**, 282–286. (2006).

36. Battogtokh, G. & Ko, Y. T. Graphene oxide-incorporated pH-responsive folate-albumin-photosensitizer nanocomplex as image-guided dual therapeutics. *J. Control Release* **234**, 10–20 (2016).

37. Zhang, C. et al. Glycyrrhetinic acid functionalized graphene oxide for mitochondria targeting and cancer treatment in vivo. *Small* **14**, 1703306 (2018).

38. Wang, H. et al. Light-controlled oxygen production and collection for sustainable photodynamic therapy in tumor hypoxia. *Biomaterials* **269**, 120621 (2021).

39. Xue, X. D. et al. Trojan Horse nanotheranostics with dual transformability and multifunctionality for highly effective cancer treatment. *Nat. Commun.* **9**, 3653 (2018).

40. Zhou, F. et al. Tumor microenvironment-activatable prodrug vesicles for nanoenabled cancer chemoimmunotherapy combining immunogenic cell death induction and CD47 blockade. *Adv Mater* **31**, e1805888 (2019).

41. Xu, B. et al. Bright and efficient light-emitting diodes based on MA/Cs double cation perovskite nanocrystals. *J. Mater. Chem. C* **5**, 6123–6128 (2017).

42. Xie, J. et al. Emerging strategies of nanomaterial-mediated tumor radiosensitization. *Adv. Mater.* **31**, e1802244 (2019).

43. Chen, W. et al. Cell membrane camouflaged hollow Prussian blue nanoparticles for synergistic photothermal-chemotherapy of cancer. *Adv. Funct. Mater.* **27**, 1605795 (2017).

44. Gandin, E., Lion, Y. & Van de Vorst, A. Quantum yield of singlet oxygen production by xanthene derivatives. *Photochem. Photobiol.* **37**, 271–278 (1983).

45. Redmond, R. W. & Gamlin, J. N. A compilation of singlet oxygen yields from biologically relevant molecules. *Photochem. Photobiol.* **70**, 391–475 (1999).

46. Kravchenko, O., Sutherland, T. C. & Heyne, B. Photobleaching of Erythrosine B in aqueous environment investigation beyond pH. *Photochem Photobiol* **98**, 49–56 (2022).

47. Clement, S., Deng, W., Camilleri, E., Wilson, B. C. & Goldys, E. M. X-ray induced singlet oxygen generation by nanoparticle-photosensitizer conjugates for photodynamic therapy: determination of singlet oxygen quantum yield. *Sci. Rep.* **6**, 19954 (2016).

48. Shrivastava, A. et al. Molecular iodine induces caspase-independent apoptosis in human breast carcinoma cells involving the mitochondria-mediated pathway. *J. Biol. Chem.* **281**, 19762–19771. (2006).

49. Yu, J. et al. Iodine conjugated Pt(IV) nanoparticles for precise chemotherapy with iodine-Pt guided computed tomography imaging and biotin-mediated tumor-targeting. *ACS Nano* **16**, 6835–6846 (2022).

50. Meng, X. et al. High-Performance self-cascade pyrite nanozymes for apoptosis-ferroptosis synergistic tumor therapy. *ACS Nano* **15**, 5735–5751 (2021).

51. Chen, W. S. Z. et al. Cell membrane camouflaged hollow Prussian blue nanoparticles for synergistic photothermal-/chemotherapy of cancer. *Adv. Funct. Mater.* **27**, 1605795 (2017).

52. Jangili, P. et al. DNA-damage-response-targeting mitochondria-activated multifunctional prodrug strategy for self-defensive tumor therapy. *Angew. Chem. Int. Ed.* **61**, e202117075 (2022).

53. Delahunty, I. et al. 7-Dehydrocholesterol encapsulated polymeric nanoparticles as a radiation-responsive sensitizer for enhancing radiation therapy. *Small* **18**, 2200710 (2022).

54. He, L., Xiao, D., Feng, J., Yao, C. & Tang, L. Induction of apoptosis of liver cancer cells by nanosecond pulsed electric fields (nsPEFs). *Med. Oncol.* **34**, 24 (2017).

55. Jia, W. et al. Brain-targeted HFn-Cu-REGO nanoplatform for site-specific delivery and manipulation of autophagy and cuproptosis in glioblastoma. *Small* **19**, e2205354 (2023).

56. Patteson, J. B. et al. Biosynthesis of fluopsin C, a copper-containing antibiotic from Pseudomonas aeruginosa. *Science* **374**, 1005–1009 (2021).

57. Rooswinkel, R. W. et al. Antiapoptotic potency of Bcl-2 proteins primarily relies on their stability, not binding selectivity. *Blood* **123**, 2806–2815. (2014).

58. Warren, C. F. A., Wong-Brown, M. W. & Bowden, N. A. BCL-2 family isoforms in apoptosis and cancer. *Cell Death Dis.* **10**, 177 (2019).

59. Liu, X. H., Chen, G. G., Vlantis, A. C., Tse, G. M. & van Hasselt, C. A. Iodine induces apoptosis via regulating MAPKs-related p53, p21, and Bcl-xL in thyroid cancer cells. *Mol. Cell Endocrinol.* **320**, 128–135 (2010).

Acknowledgements

Author contributions

X.M., N.L., Q.Y., and H.C. conceived the idea and supervised the research; X.M., N.L., Q.Y., P.L., H.D., M.X., F.R., Z.S., K.H., S.M. performed the synthesis and characterization, investigations in vitro and in vivo; X.M., N.L., Q.Y., and H.C. analyzed the data; X.M., N.L., Q.Y., and H.C. co-wrote the paper. All authors discussed the results and commented on the manuscript.

Competing interests

The authors declare no competing interests.

Additional information

Supplementary information The online version contains supplementary material available at https://doi.org/10.1038/s41467-024-52278-6.

Correspondence and requests for materials should be addressed to Hongmin Chen.

Peer review information *Nature Communications* thanks Javier Troyano, and the other, anonymous, reviewer(s) for their contribution to the peer review of this work. A peer review file is available.

Reprints and permissions information is available at http://www.nature.com/reprints